Available online at www.sciencedirect.com
ScienceDirect
Journal of Sound and Vibration 308 (2007) 28–43
JOURNAL OF SOUND AND VIBRATION
www.elsevier.com/locate/jsvi

A turbulent inflow model based on velocity modulation

Stephen A. Huyer*, David Beal

Naval Undersea Warfare Center, Propulsion and Motion Control Branch, Code 8233, Building 1302/2, Newport, RI 02841, USA

Received 7 October 2005; received in revised form 25 October 2006; accepted 27 June 2007
Available online 5 September 2007

Abstract

This article presents a novel turbulent inflow model based on modulation of the velocity field for use with time-domain propulsor calculations. Given an experimental mean and rms turbulent inflow, a model can be constructed by modulating the velocity field over a range of frequencies. Assuming the turbulence is homogeneous, the inflow can be constructed as a Fourier series where the frequencies can also be modulated to smooth the broadband output. To demonstrate the effectiveness of the model, experimental inflow velocity data were acquired for an upstream stator, downstream rotor configuration mounted on an undersea vehicle afterbody. Two main sources of turbulence originated from the vorticity shed from the stator wakes and the boundary layer vorticity produced on the hull body. Three-dimensional, unsteady velocity data were acquired using hot-wire anemometry and reduced to provide mean and rms velocity values. Time-series data were processed to provide velocity power spectra used to calibrate the model. Simulations were performed using a modified version of the propulsor unsteady flow code capable of computing fully turbulent inflows. This solver models the propulsor blade as a vortex lattice and sheds the vorticity into the wake to solve the unsteady potential flow. The no-flux boundary conditions are satisfied at the lattice control points and the resulting unsteady circulation is a function of the instantaneous inflow velocity field over the blade. Vorticity is shed into the wake to account for the full time history of the inflow velocity field. To demonstrate the full effectiveness of the model, computed surface pressure data were exported to a code to compute the far-field radiated noise (both tonal and broadband). Simulated data were compared with experimentally obtained noise data with favorable results. Applications of this methodology in the incompressible flow domain include broadband analysis of propulsor-radiated noise on undersea vehicles and radiator fan noise in cars.
Published by Elsevier Ltd.

1. Introduction

Propellers that operate on undersea vehicles ingest a complex unsteady inflow, which greatly affects the unsteady forces and radiated noise. This unsteady inflow is generated by the wakes and boundary layers produced by upstream control surfaces and stators, which combine with the hull boundary layer to produce a very complex spatially and temporally varying inflow. As the propeller encounters coherent wakes, there is an unsteady response resulting in periodic, narrowband forces resulting in an acoustic signature that may be used to characterize the vehicle. The turbulence in the wake can further excite the narrowband forces due to the inherent unsteadiness. The hull boundary layer contains turbulent eddies of various length scales that are

*Corresponding author. Tel.: +1 401 832 2768; fax: +1 401 832 6202.
E-mail address: huyersa@npt.nuwc.navy.mil (S.A. Huyer).

0022-460X/$ - see front matter Published by Elsevier Ltd.
doi:10.1016/j.jsv.2007.06.051

ingested into the propeller. This results in a broadband type of response function that increases the overall noise. The ability to properly model the complex turbulent inflow is vital to predict the unsteady hydrodynamic forces and subsequent radiated noise.

Previous work on turbulent inflow models as applied to propulsors has treated the problem in the frequency (wavenumber) domain (see, for example, [1–3]). This requires knowledge of the turbulent spectra as well as the spatial correlation in order to properly define the inflow. Usually, this is very difficult to obtain experimentally, although computational fluid dynamics (CFD) may be used. For example, Lysak and Brungart [3] recently presented a method utilizing the Von Karman model to predict the energy spectrum based on k–ε output from a CFD solution. For isotropic turbulence, the velocity spectrum can be obtained from the energy spectrum. The Sears gust response function is then used to predict the unsteady response of the propeller.

Time-domain methods offer an alternative approach. Vortex lattice methods may be used to model the propeller blades and wake as suggested by Kerwin [4]. The full three-dimensional (3-D) geometry of the propeller blades can be discretized with the potential flow equations solved at the blade lattice points. The circulation of the vortex lattice is then defined at the control points and wake. The advantage to this approach is that 3-D effects are included (which the Sears gust function does not account for). In this method, the spatially unsteady inflow is used as boundary conditions to compute the blade circulation and unsteady loading. This method was extended by Huyer and Snarski [5] for examination of fully turbulent inflows (e.g. time-dependant flow).

Huyer and Kuklinski [6] conducted simulations to examine the effect of modulating the propeller inflow and the subsequent blade force response. They found that modulating the inflow at a given frequency resulted in a corresponding force response at the same frequency. By modulating the inflow for a spectrum of frequencies, the resulting response was broadband in nature and qualitatively similar to the response expected from turbulence ingestion. This paper presents a refined method for a broadband turbulent inflow model that may be used for time-dependant flow simulations.

For this investigation, a modified version of the propulsor unsteady flow code was used. This code utilizes potential flow methods to compute the 3-D unsteady lift forces generated by a propulsor [4,7,8]. The propulsor unsteady flow code employs the current state of the art lifting surface theory and assumes that the propulsor can be modeled as a set of thin blades arranged symmetrically about a common axis. The code was modified [5] so that time-dependant inflows could be examined. Computations are now made over multiple blade rotations and the forces and pressures are computed on each individual blade. Fully unsteady, turbulent inflows can be used as surface boundary conditions. In these simulations, experimental data [9,10] are used as boundary conditions to compute the unsteady forces. Based on these data, a turbulent inflow model was constructed and the blade force response and radiated noise computed. Comparisons with radiated noise measurements demonstrate the overall effectiveness of the model.

2. Methodology

2.1. Experimental inflow measurements

Numerical simulations utilize the experimentally defined inflow as boundary conditions. A non-ducted six blade propeller was situated downstream of eight stators [11]. The stator wakes produce a velocity defect that the propeller responds to. By placing the propulsor on a vehicle afterbody, a turbulent hull boundary layer was produced that the propulsor also responds to. Fig. 1 shows the experimental configuration. Details of the experimental methodology will be summarized here. For more detail, [9,10] may be consulted.

Experiments were previously conducted at the Naval Undersea Warfare Center (NUWC) in the open jet wind tunnel facility and have previously been described in Ref. [12]. The wind tunnel has a circular exit 4 ft in diameter, maximum speed of 200 ft/s, average turbulence level of 0.3%, and spatial uniformity of 0.5% at 120 ft/s. The test area is also located in an anechoic chamber so radiated noise measurements can be made. The propulsor configuration was mounted on a 53.34 cm (21 in) unmanned undersea vehicle full-scale model and sting mounted at the centerline of the wind tunnel. Measurements used for comparisons with the current simulations were conducted for a freestream velocity of 29.3 m/s. The propulsor was mounted on an afterbody

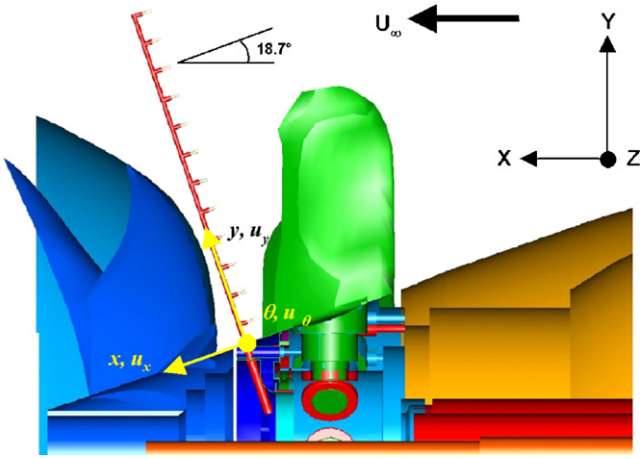

Fig. 1. Stator and propulsor blade configuration. The local and global coordinate system is displayed. Artwork reproduced from Muench [9] with permission.

connected to a quiet electric spinner assembly. Hama-type boundary layer trips were attached to the stator and propeller blades to ensure turbulent boundary layer flow. The trips were placed at 1/4 chord along the entire span of the blades.

Hot-wire anemometry measured the unsteady, 3-D velocity field using u–v and u–w x-wire probes constructed by TSI Incorporated. Data were anti-alias filtered at 3 kHz and sampled at 10 kHz for a total of 8192 samples. Data were post-processed using MATLAB software to provide mean and rms velocities for all three directions. A rotating hub mechanism contained six probe sockets spaced 60° apart which were situated normal to the body between the stator and propeller blades. This resulted in a measurement angle of 18.7° relative to the centerline perpendicular. A stepper motor was designed to rotate the mechanism in 0.6° increments with an error of 0.01° for a total of 600 measurements. Measurements were taken at 12 stations in the radial direction from 2 to 24 cm above the body surface in 2 cm increments for a total of 7200 points in the radial-circumferential plane.

Fig. 2 shows the mean experimental inflow (a) and the rms (b) for the axial component. Velocities are non-dimensionalized by the freestream velocity. The mean velocity highlights the eight stator wakes and the growth of the hull boundary layer. Velocity defects in the wake are typically 80% of maximum values in the upper boundary layer. The rms figure highlights the turbulent wakes even better, where sharp increases of 10% are seen in the stator wake. Also, the boundary layer appears more clearly and extends out to $r/R_{\text{prop}} = 0.8$.

The experimental propulsor inflow was extrapolated downstream to provide boundary conditions for the propulsor unsteady flow code. Experimentally, the total inflow was measured and includes the induced velocity due to the propeller. The code requires the effective velocity (total velocity minus the propeller induced velocity). The induced velocity due to the propeller was then subtracted off the experimental inflow to obtain the effective inflow used as boundary conditions. Since the shape of the hub is conical, the streamlines and subsequent fluid momentum will be altered accordingly. To model this effect, the outermost measurement location was assumed to have a primarily axial velocity. This suggests that the streamlines are parallel to the x-axis, so the outer streamline cone can be defined. Since the hub is cone shaped and converges to a point, the effective cross-sectional area of all the stream tubes in a given plane must increase. In the measurement plane, the radial locations are spaced equally. As a zeroth-order approximation, it was assumed that the streamtubes would diverge uniformly so that at downstream locations, the radial locations of the extrapolated data are also spaced uniformly. To conserve mass, this model was then used to reflect the resultant loss in flow velocity (since area increases) as the experimental inflow is extrapolated downstream. This may be expressed mathematically as

$$\left[\vec{\mathbf{V}}_i(r_i - r_{i-1})\,\mathrm{d}\theta\right]_n = \left[\vec{\mathbf{V}}_i(r_i - r_{i-1})\,\mathrm{d}\theta\right]_{n-1}, \tag{1}$$

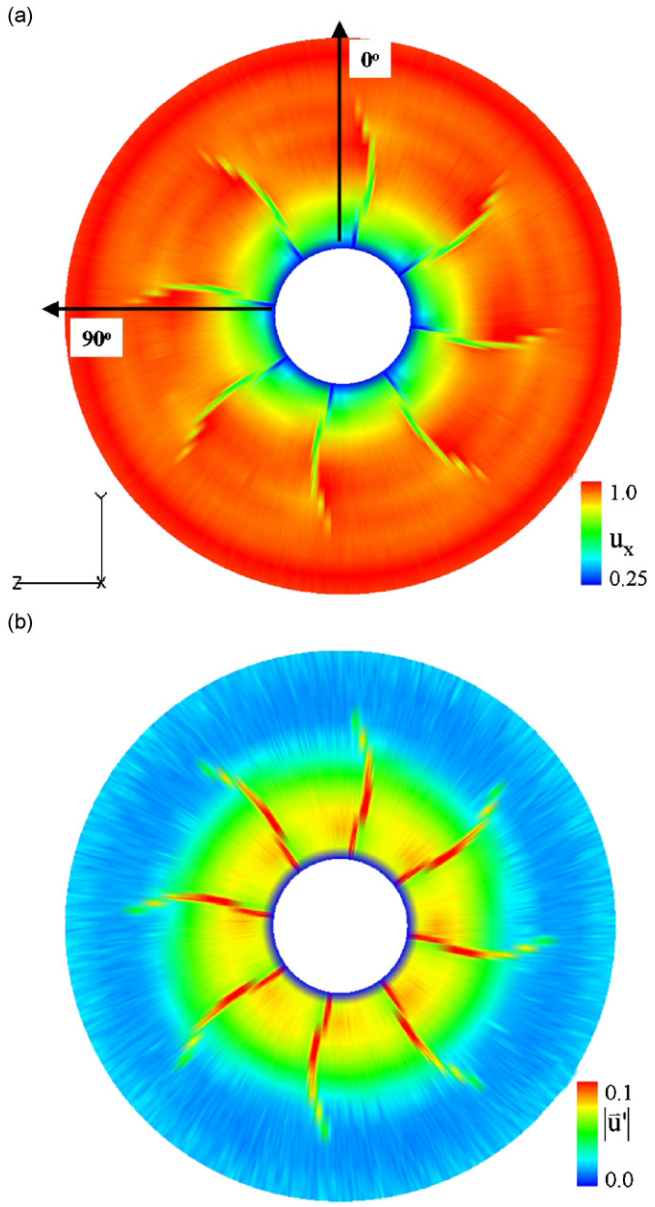

Fig. 2. (a) Experimental mean inflow velocity field and (b) rms inflow velocity field for the axial velocity component.

where $\vec{\mathbf{V}}$ is the velocity, r is the radial location, i refers to the radial index, $d\theta$ is the angular increment, and n refers to the extrapolated plane location. Also, the effective spreading of the stator wakes was modeled as well to reflect the spreading of the stator wake vorticity. Fig. 3a shows the resulting extrapolation to points downstream. The furthest upstream plane is the actual location of the experimental measurements, the second plane is immediately aft of the propulsor, and the furthest downstream plane is located two propulsor diameters downstream. Notice the wake spreading at the downstream inflow plane.

2.2. *Propulsor unsteady flow code*

The propulsor unsteady flow code is based on lifting surface theory and was developed at the Massachusetts Institute of Technology under the direction of Professor Justin Kerwin. For more detailed information on the theory and algorithms, the reader is referred to [4,7,8].

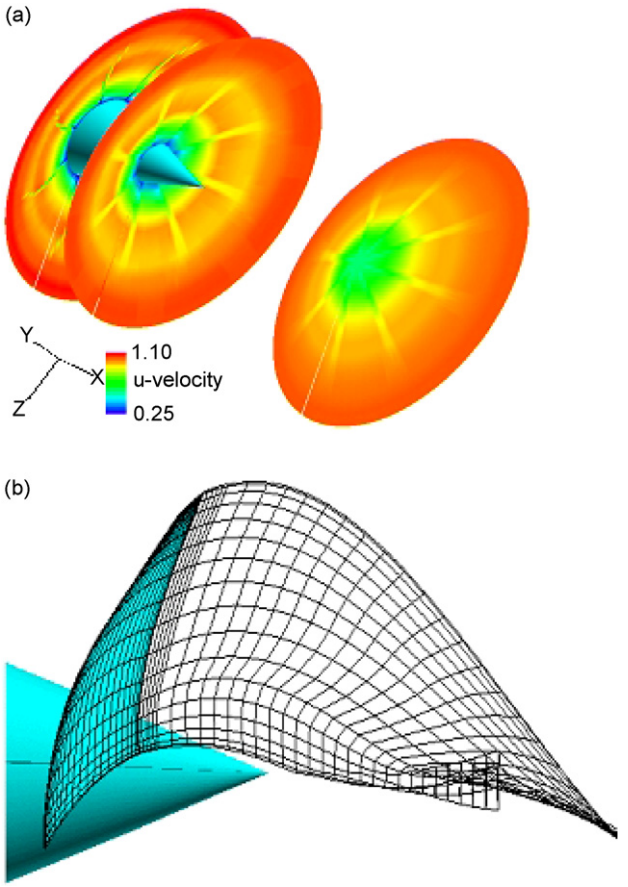

Fig. 3. (a) Experimental (first plane) and extrapolated inflow mean velocity field and (b) PUF computational grid.

The blade geometry is generated and blade coordinates output in the form of tabular data, which are then uniquely defined using B-spline surface meshes. B-splines allow the surface of the blade to be described by very few points. The blade surface may then be discretized so the spatial resolution is sufficient for an accurate computation of the flow. In the present test cases, 17 points in the spanwise and 20 points in the chordwise direction are used to describe the blade surface (see Fig. 3b). It is assumed that all blades are identical and evenly spaced about the hub.

2.3. *Lifting surface theory*

The flow is assumed to be incompressible and inviscid and the domain is assumed to be unbounded. The propulsor is assumed to consist of a set of thin blades at small angles of attack so separated flow effects may be neglected. These assumptions allow for the vorticity to be confined to the surface and the wake with the remainder of the flow assumed irrotational. These assumptions allow for the use of potential flow theory. The potential flow problem satisfies Laplace's equation:

$$\nabla^2\varphi = 0, \tag{2}$$

where φ is the velocity potential and the perturbation velocity due to the potential flow is defined as

$$\vec{\mathbf{V}}_p = \nabla\varphi. \tag{3}$$

In the present formulation, the contribution to the velocity potential is from the surface only. For a point $\vec{x}$, source point $\vec{\xi}$, surface S and surface normal $\vec{\mathbf{n}}$, this is defined as

$$-2\pi\varphi(\vec{x}) = \int_S \int \frac{1}{|\vec{x}-\vec{\xi}|}\vec{\mathbf{n}}(\vec{\xi})\cdot\nabla_{\xi\varphi}(\vec{\xi}) - \varphi(\vec{\xi})\,\vec{\mathbf{n}}(\vec{\xi})\cdot\nabla_{\xi}\frac{1}{|\vec{x}-\vec{\xi}|}\,\mathrm{d}S. \tag{4}$$

Taking the gradient of (4) with respect to $\vec{x}$ yields the perturbation velocity. Assuming that the surface is infinitely thin, the upper and lower surfaces of the blade coincide so the governing set of equations becomes

$$\int_{S_B}\int \mu(\vec{\xi})\,\vec{\mathbf{n}}(\vec{x})\cdot\left[\nabla_x\left(\vec{\mathbf{n}}(\vec{\xi})\cdot\nabla_{\xi}\frac{1}{|\vec{x}-\vec{\xi}|}\right)\right]\mathrm{d}S_B$$
$$= \int_{S_W}\int \mu_W(\vec{\xi})\,\vec{\mathbf{n}}(\vec{x})\cdot\left[\nabla_x\left(\vec{\mathbf{n}}(\vec{\xi})\cdot\nabla_{\xi}\frac{1}{|\vec{x}-\vec{\xi}|}\right)\right]\mathrm{d}S_W - 2\pi\,\vec{\mathbf{n}}(\vec{x})\cdot\vec{\mathbf{u}}_{in}(\vec{x}). \tag{5}$$

Here, $\mu(\vec{\xi})$ is defined as the potential jump across the surface and $\mu_w(\vec{\xi})$ is the potential jump in the wake, the subscripts B and W refer to the blade and wake, respectively, $\vec{\mathbf{u}}_{in}$ is the inflow velocity. To numerically describe the flow, the blade surface is discretized to a series of sources and distribution of vorticity on the camber surface and wake and the normal velocity (no-flux) boundary conditions are satisfied. The sources generate a jump in normal velocity to effectively account for blade thickness. The source strengths are solved for only once and the effect of the vorticity is assumed negligible. The vorticity distribution on the surface is solved for according to Eq. (5) and the vorticity in the wake is assumed as a given. To solve Eq. (5), the vorticity is assumed to be composed of filaments that encircle each panel of constant strength consistent with Kelvin's theorem. The integral expression may be evaluated analytically for straight vortex filaments and the solution provided in Ref. [7]. Eq. (5) forms a matrix set of equations that are solved at each time step. To avoid forming the solution matrix on every time step, the location of the first wake panel is kept a constant distance downstream and is based on the circumferentially averaged inflow velocity and blade rotational velocity.

The Kutta condition requires the velocity at the trailing edge to be finite. To satisfy this, an implicit Kutta condition is imposed where control points are placed at the trailing edge and the boundary condition $\vec{\mathbf{n}}(\vec{x})\cdot\vec{\mathbf{u}}_{in}(\vec{x})$ is satisfied. Also, the dynamic boundary condition states that there is no pressure jump across the trailing vortex wake. This is satisfied by requiring that the vortex sheets are advected by the local flow velocity.

To account for the vortex wake, the propulsor unsteady flow code defines a transitional wake and ultimate wake. The transitional wake geometry is formed assuming that the wake panels are advected downstream using the circumferentially averaged inflow and corresponding blade rotational velocity. The wake then forms a helical structure and the panel representation is used during solution of Eq. (5). Wake contraction is modeled with a user specified wake contraction angle. Vorticity is shed at each time step to form the transitional wake. Panels are shed downstream before merging with the ultimate wake, whose location is user specified (tests show one propulsor radius downstream results in minimal errors). At the ultimate wake, each trailing vortex line from each blade is merged into an infinite-bladed helical vortex whose radius matches that of the trailing vortex at the end of the transition wake.

The code computes the blade forces based on the effects of surface pressure force, viscous force, leading edge suction forces and unsteady force. The viscous forces account for skin friction due to finite viscosity and the leading edge suction forces are required due to the assumption of zero blade thickness. Viscous forces are computed via a user supplied empirical drag coefficient for the blade. The pressure force is obtained from Joukowski's law for individual panels and then integrated over the entire blade surface. This force may be expressed as

$$\mathrm{d}\vec{\mathbf{F}}_J = \rho\,\mathrm{d}A(\vec{\mathbf{V}}\times(\vec{\mathbf{n}}\times\vec{\nabla}_s\mu)). \tag{6}$$

Here, $\vec{\mathbf{V}}$ is the total velocity at the panel control points, ρ the density, $\mathrm{d}A$ the panel area and $\vec{\mathbf{n}}$ the panel unit normal. The gradient of the potential jump along the surface governs the blade force.

The unsteady velocity potential contribution to the force is given by the derivative of the velocity potential. Since the source contribution is steady, the only contribution to the potential is from the vortices. Since the

blade forces are computed after the solution has converged, the code uses a central five-point differentiation formula to numerically solve the unsteady potential contribution.

2.4. Propulsor unsteady flow code modifications

The propulsor unsteady flow code was written to solve for a spatially varying but temporally steady inflow. Essentially, the only quantities that needed to be computed were for a single blade (referred to as the key blade) over one propeller revolution. The matrix formulation was already set up to compute the fully coupled problem solving for the circulation on all the blades at each time step throughout the blade rotation according to Eq. (5). It was possible to then compute the circulation on all the blades. At each time step, the vorticity was then shed into the wake and the wake vorticity was unique for each blade. To account for multiple rotations, the computation was converged for the first two blade rotations only. During this time, vorticity was shed into the wake and was advected sufficiently far downstream so the ultimate wake was reached. Since the solution converged and the wake was established, it was not necessary to converge the solution for subsequent blade rotations. Therefore, further flow evolution due to additional blade revolutions could be computed by implementing the boundary conditions, solve Eq. (5), and shed the resultant trailing edge vorticity into the wake. Once all the circulation values are known throughout all propeller revolutions over all blades, the induced velocities contributing to the blade force and surface pressure were computed for every blade (instead of the key blade only).

2.5. Modulated inflow

The inflow can be modulated according to the formula:

$$\vec{\mathbf{u}}_{\text{inflow}}(t) = \left(A_{\text{perturb}} \sin\left(2\pi \frac{t}{T_{\text{prop}}} f(t)\right)\right) f_{\text{mean}} + f_{\text{perturb}} \sin\left(2\pi \frac{t}{T_{\text{mod}}}\right). \tag{7}$$

Here, A_{perturb} the perturbation amplitude of the disturbance, T_{prop} the propeller shaft rotation period, f_{mean} the mean modulation frequency, and f_{perturb} the time-varying term to modulate the frequency, $f(t)$ and T_{mod} the modulation period. All frequencies are normalized by the shaft rate, f_{SR}. Fig. 4 shows the perturbation velocity for the case where $A_{\text{perturb}} = 0.1$, $f(t) =$ constant ($f_{\text{mean}} = 4$), and where $f_{\text{mean}} = 4$, $f_{\text{perturb}} = 2$ with $T_{\text{mod}} = T_{\text{prop}}$. Fig. 5 shows the effect for a range of T_{mod} on the velocity power spectra. For low values of T_{mod}, there are more fluctuations in the spectra. As T_{mod} is increased, the fluctuations are reduced and the spectra become flatter over the range of frequencies due to modulation amplitude (from $f/f_{\text{SR}} = 2.0$–6.0).

2.6. Experimental velocity spectra

Time-series velocity data were reduced using MatLab software in order to produce velocity power spectra for the axial, radial and tangential velocity components. Experimental data were acquired at a sampling frequency of 10,000 Hz with 8192 samples collected to generate the data. When non-dimensionalized, this produced 366 samples over a single propeller rotation with data collected for 22 rotations. This translates to a frequency resolution of approximately 0.4 and Nyquist frequency of 170. A total of 8 samples were averaged to obtain the velocity spectra. Data were processed using a Hanning window and were corrected for a 1 Hz bandwidth.

Fig. 6 shows the velocity power spectra taken at a radial position, $r/R_{\text{prop}} = 0.65$ (R_{prop} is the propeller radius). These data were taken between two stators to estimate the spectra associated with the hull boundary layer. Data are plotted on a logarithmic scale for power and a linear scale for frequency. As can be seen, there appears to be a linear decrease in power as a function of frequency for the axial component. The spectra appears to be flat out to $f/f_{\text{SR}} = 20$ for the radial component and $f/f_{\text{SR}} = 10$ for the tangential component. At the higher frequencies, the spectra for all three components appear similar. In all velocity spectra processed, a definite blade rate tonal ($f/f_{\text{SR}} = 6$) appears. This is due to the induced velocity component on the velocity field as the propeller blades pass by the measurement point.

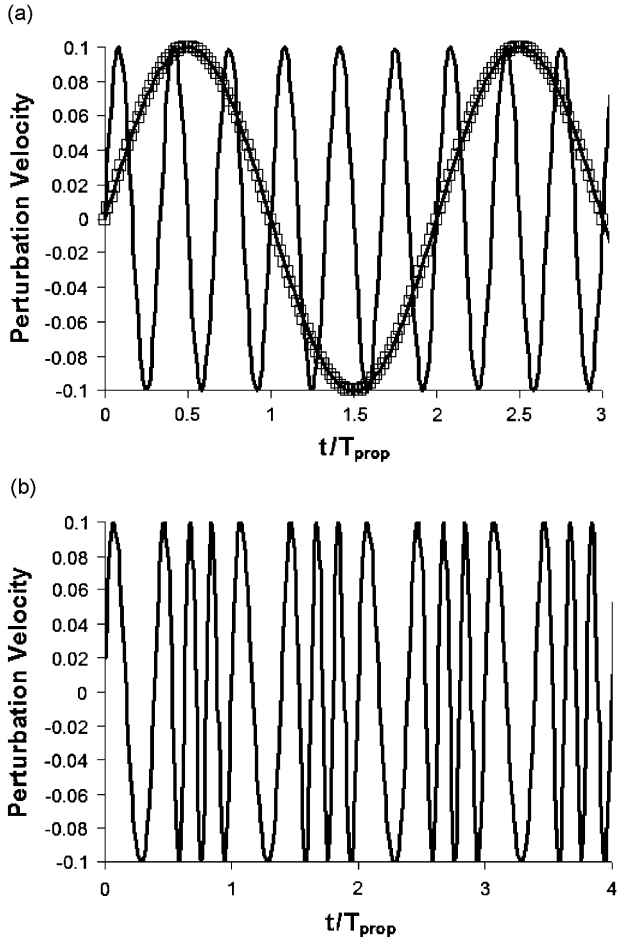

Fig. 4. Modulated inflow perturbation velocity with $A_{\text{perturb}} = 0.1$ for (a) constant frequency (—— $f/f_{SR} = 0.5$, —□— $f/f_{SR} = 3.0$), (b) modulated frequency with $f_{\text{mean}}/f_{SR} = 4$, $f_{\text{perturb}} = 2$, and $T_{\text{mod}} = T_{\text{prop}}$.

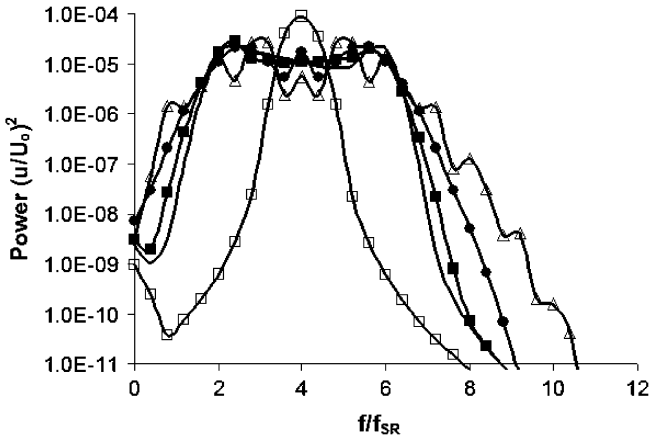

Fig. 5. Velocity power spectra illustrating the effect of modulation period for $f_{\text{mean}}/f_{SR} = 4$, $f_{\text{perturb}} = 2$ and $T_{\text{prop}} = 1.0$. —□— $f/f_{SR} = 4$ (constant f), —△— $T_{\text{mod}} = 1$, —●— $T_{\text{mod}} = 2$, —■— $T_{\text{mod}} = 4$, —— $T_{\text{mod}} = 8$.

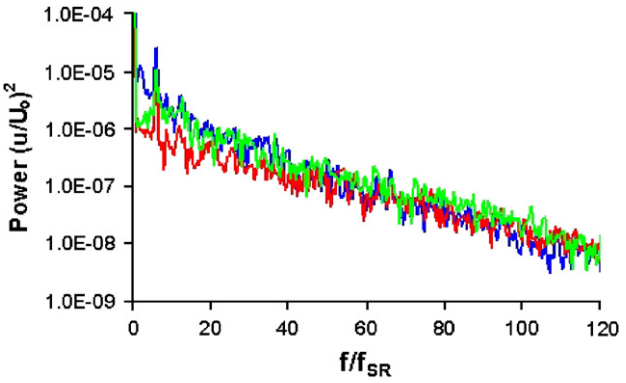

Fig. 6. Velocity power spectra based on experimental data taken in the middle of the hull boundary layer at $r/R_{\text{prop}} = 0.65$ midway between two stators for the axial, radial and tangential velocity components.

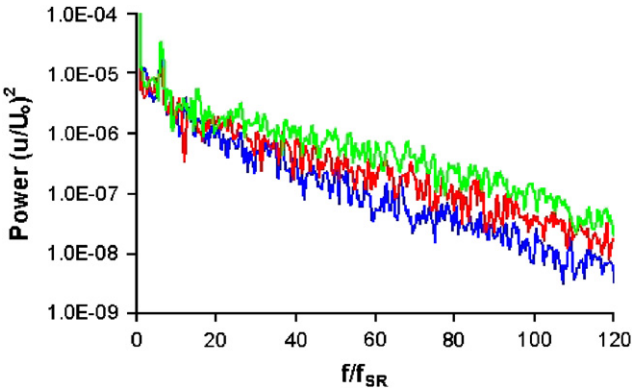

Fig. 7. Velocity power spectra based on experimental data taken in the middle of the hull boundary layer at $r/R_{\text{prop}} = 0.65$ for the axial velocity component. between two stators, stator wake center and wake edge.

Fig. 7 shows the difference in spectra for stations between the two stators (complete hull boundary layer effect) for the stator wake center, and at the wake edge for the axial velocity component. In each case, there appears a linear decrease in power as a function of frequency. The slope appears greater for the hull boundary layer compared with the stator wake. The wake edge slope appears half-way between the hull boundary layer and wake center. In all cases, it appears that the dc offsets (very low frequencies) are similar.

Axial velocity spectra taken at various radial stations in the hull boundary layer are plotted in Fig. 8. Values for the axial turbulence (u'_x) are shown in the legend. In the lower boundary layer, u'_x and hence the velocity spectra are quite similar. Toward the outer boundary layer, it appears that the spectra, for a 50% decrease in turbulence, are shifted downward by one order of magnitude in power. At $r/R_{\text{prop}} = 0.96$, the probe is no longer in the hull boundary layer and freestream turbulence is measured. In this case, the high frequency components are effectively zero (in the numerical processing noise region).

2.7. Modulated velocity turbulent inflow model

In the turbulent inflow model, the velocity is computed for each blade point along its trajectory in time. The turbulent signal consists of a summation of sinusoids with random phase and amplitudes then re-scaled so that the rms value of the velocity component is unity. The number of sinusoids used in the sum was chosen to completely fill the resolution of a Fourier transform of the signal, proportional to the time resolution and total

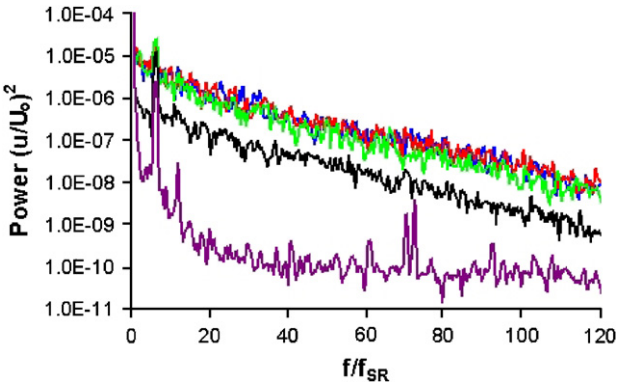

Fig. 8. Velocity power spectra based on experimental data taken in the hull boundary layer midway between two stators for the axial velocity component at various radial locations throughout the boundary layer. $r/R_{\text{prop}} = 0.39$ ($u'_x = 5.44\%$), $r/R_{\text{prop}} = 0.47$ ($u'_x = 5.58\%$), $r/R_{\text{prop}} = 0.65$ ($u'_x = 5.0\%$), $r/R_{\text{prop}} = 0.82$ ($u'_x = 2.33\%$), $r/R_{\text{prop}} = 0.98$ ($u'_x = 1.04\%$).

length of the simulation. For example, if the time resolution consists of 180 points over a single blade rotation, the Nyquist criteria allows for computation of frequencies of 90 (normalized by the shaft rate) or less. Eq. (7) is modified so the total velocity inflow for each blade point at each point in time is determined by

$$\vec{\mathbf{u}}_{\text{inflow}}(x,r,\theta,t) = \vec{\mathbf{u}}_{\text{exp}}(x,r,\theta) + \vec{\mathbf{u}}'_{\text{exp}}(x,r,\theta) \sum_{n=1}^{n=\text{NTSR}\,N/2} a_n \sin\left(2\pi \frac{t}{T_{\text{prop}}} f(t) + \psi_n\right), \tag{8}$$

where $\vec{\mathbf{u}}_{\text{inflow}}(t)$ is the equivalent time-series turbulent inflow and $\vec{\mathbf{u}}_{\text{exp}}$ and $\vec{\mathbf{u}}'_{\text{exp}}$ are the mean and RMS turbulent velocity magnitudes determined based on experimental or computational data (experimental for the present studies). $\vec{\mathbf{u}}_{\text{exp}}$ and $\mathbf{u}'_{\text{exp}}$ are found by interpolating the current axial, radial and circumferential position of the blade point in the inflow plane into the experimental mean and turbulent velocity magnitude data. NTSR is the number of time steps per revolution (set to 180 for these trials), N is the number of revolutions in the simulation and ψ_n is a random phase value between 0 and 2π. In order to avoid exceptional spikes in turbulent velocity, the summation was limited to an amplitude of 20.

For a flat spectra, the coefficients, a_n, are constant across the frequency spectra. As was shown, the experimental velocity spectra show an approximate linear (in a logarithmic sense) decrease in power as a function of frequency. Therefore, in order to calibrate the model, experimental spectral data are used to approximate the frequency dependence of a_n. It was found that the following function fit well with the experimental data in terms of slope and dropoff at the higher frequencies:

$$a_n(e^{-c_{\text{turb}} f_{\text{mean}}}), \tag{9}$$

here, c_{turb} is a coefficient that depends on the turbulent inflow characteristic. For the hull boundary layer, $c_{\text{turb}} = 0.04$ and for the stator wake, $c_{\text{turb}} = 0.03$. Owing to the extreme sharpness of the stator wake, a simple measure of turbulent velocity gradient was used to identify the location of the stator wake vs. the hull boundary layer. Finally, the decrease in power as the outer boundary layer is approached is modeled by decreasing the amplitudes using the following:

$$\begin{aligned} &a_n(e^{-c_{\text{turb}} f_{\text{mean}}}) \quad \text{for } u'_x > 0.05, \\ &a_n(e^{-c_{\text{turb}} f_{\text{mean}}})\left(1.0 - \frac{0.05 - u'_x}{0.035}\right)^3 \quad \text{for } 0.015 < u'_x < 0.05, \\ &a_n = 0 \quad \text{for } u'_x < 0.015. \end{aligned} \tag{10}$$

Fig. 9 shows a comparison of the experimental data with the axial velocity spectra obtained by combining Eqs. (8) and (10). For the simulations, NTSR = 180 over a total of 30 propeller revolutions for a total of 5400

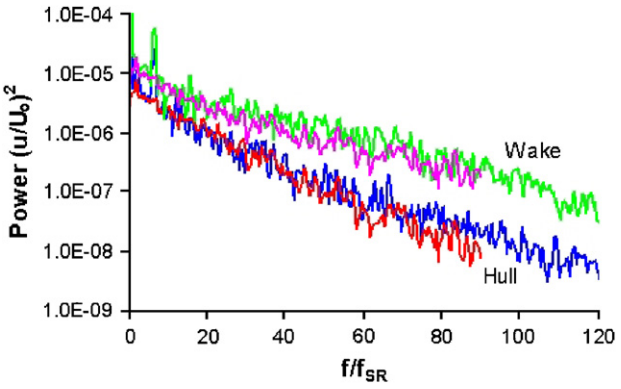

Fig. 9. Velocity power spectra comparing simulated and experimental velocity spectra for the hull boundary layer and stator wake. Experiment (hull), simulation (hull), experiment (wake), simulation (wake).

samples. f_{mean} was increased incrementally from 0.5–90, $f_{\text{perturb}} = 0.5$ and $T_{\text{mod}} = 8T_{\text{prop}}$. Each discrete Fourier transform consisted of 450 points and 12 consecutive transform's were averaged. The resulting frequency resolution was 0.4 with a Nyquist frequency of 90. In the simulations, the axial turbulence, $u'_x = 0.053$ for the boundary layer component and 0.083 for the wake component. As can be seen, the simulated velocity spectra are quite comparable with the experimental data.

3. Results

In all cases, non-dimensional quantities are used. The velocities are non-dimensionalized by the freestream velocity and all length scales are non-dimensionalized by the propulsor radius. The experimental inflow data set used for the surface boundary conditions is the 29.3 m/s freestream velocity case. Axial and side force coefficient data are presented (C_{fx} and C_{fy}). Here, $C_{fx} = F_x/(1/2\rho U_0^2 \pi R_{\text{prop}}^2)$ where U_0 is the freestream velocity. Coefficient data are formulated similarly for the other components. Computations were performed over thirty propeller rotations with each rotation cycle consisting of 180 time steps. Power spectra were also computed based on the unsteady axial and side forces using a MatLab discrete Fourier transform algorithm. Spectra were computed using a Hanning window function over the entire time series resulting in a frequency bandwidth of 1/6 (normalized by f_{SR}). Unless otherwise noted all time scales are assumed normalized by T_{prop} and all frequencies by f_{SR}. The length of the discrete Fourier transform sample was 1800. Combined with an effective sampling frequency of 180, a frequency resolution of 0.1 and Nyquist frequency of 90 was obtained. Three consecutive runs were averaged to provide the final power spectra traces.

Single blade time-series force and power spectra are shown in Fig. 10. Axial and side forces are both plotted for the turbulent inflow model cases as well as the baseline case for mean experimental inflow only. Baseline forces clearly show the effect of the wakes as an 8/rev force and can clearly be seen in the time series. The forces associated with the turbulent inflow model reflect no obvious periodic patterns. This can be seen better in the power spectra plots. Here, the baseline case reflects the base harmonic (8/rev) as well as the higher harmonics. The turbulent inflow model shows a clear 8/rev, but the broadband turbulence obfuscates the effect of the higher harmonics.

Fig. 11 plots the time-series global forces taken as a summation of the forces over the six blades. Again, the periodicity is clear for the baseline case—especially for the unsteady side forces, where the blade rate (6/rev) frequency is clear. The turbulent inflow model, however, results in a seemingly random signal. Fig. 12 shows the axial and side force frequency spectra. The baseline case highlights the base blade rate tonal and the associated higher harmonics. The turbulent inflow model, however, does not demonstrate any tonal behavior. Rather, it appears the broadband effect is sufficiently above the base tonals to obfuscate them.

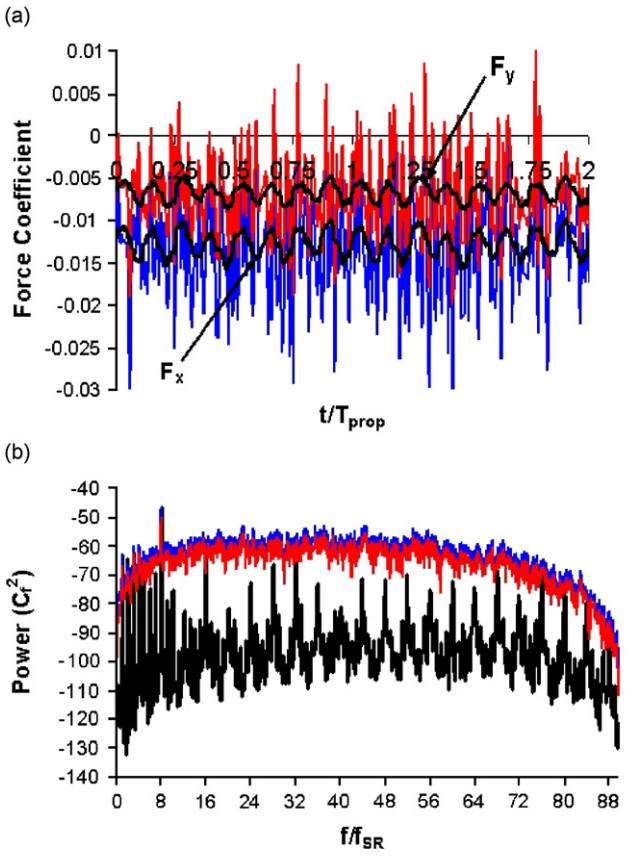

Fig. 10. Computed local axial and side force time series (a) and power spectra (b) for the baseline (no modulation) and turbulent inflow model test cases. Single blade forces only. ——— F_{xloc}, ——— F_{yloc}, ——— Baseline force values.

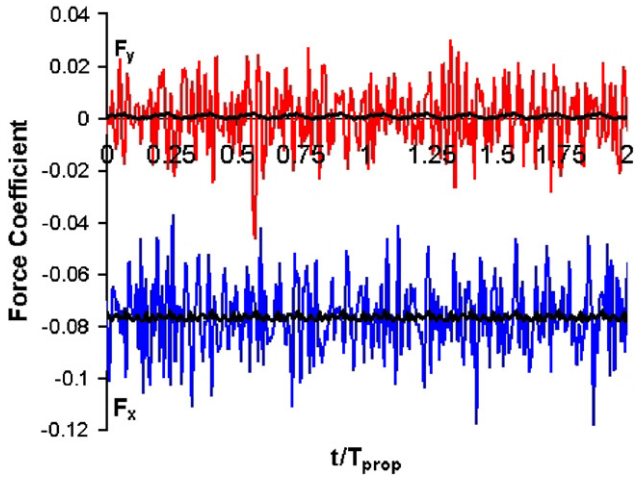

Fig. 11. Computed global axial and side force time series for the baseline (no modulation) and turbulent inflow model test cases for the six-blade rotor configuration. ——— F_x, ——— F_y, ——— Baseline force values.

Radiated noise was computed according to Goldstein [13]. His method is summarized here. The vortex lattice established for the propulsor unsteady flow code runs effectively provides the blade surface grid where pressure is computed. The product of pressure and area then provides the local elemental force for a single

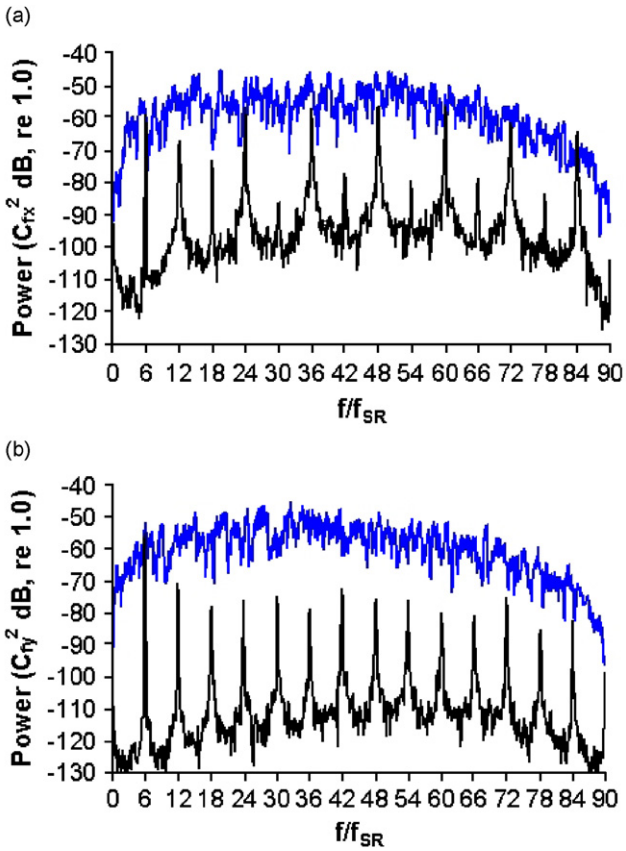

Fig. 12. Computed global axial (a) and side force (b) power spectra for the baseline (no modulation) and turbulent inflow model test cases for the six-blade rotor configuration. —— Turbulent inflow, —— Baseline.

panel. His method computes the far-field acoustic pressure based on this elemental force using a Green's function approach. The acoustic pressure at a given field point is then the summation of all the elemental forces over all of the blades.

The simulated radiated noise was then processed to obtain the frequency spectra using a method nearly identical to that of the forces and the results are presented in Fig. 13. The exception was four consecutive runs were averaged to provide a total of 12 averages for the spectra. Experimental data were obtained [9] and were taken at various stations and scaled to 1 m. A typical radiated noise signal is shown. Experimental data were sampled at 50 kHz for 78 s. In non-dimensional terms, this resulted in an effective sample rate of 1830 samples per propeller revolution over 2130 revolutions. For the discrete Fourier transform processing, the number of samples was 20,480, equivalent to data over 11 revolutions. The resulting frequency resolution was 0.09 with Nyquist frequency of 930. The large amount of data allowed for several averages to smooth out the profile. The experimental data shown were averaged for 50 consecutive runs. In Fig. 13a, the mean experimental inflow case is compared with the turbulent inflow model to highlight the broadband and tonal components. As can be seen, tonals above the third blade rate ($f/f_{SR} = 28$) are obfuscated by the broadband effect. In Fig. 13b, turbulent inflow model simulations are compared directly with the experimental data. As can be seen, the experimental data is much "smoother" compared with the simulated data. This was found to be due to the fact that 50 averages were used to assemble the experimental data whereas only three were used for the simulated data. The average levels of the broadband component, however, are equivalent as are the first two blade rate tonals. The simulated data do not reproduce blade rates from three to ten as measured experimentally. This may be caused by the fact that the higher blade rate tones produced by the mean experimental inflow are less compared with the broadband signal. It is also possible that physically, the

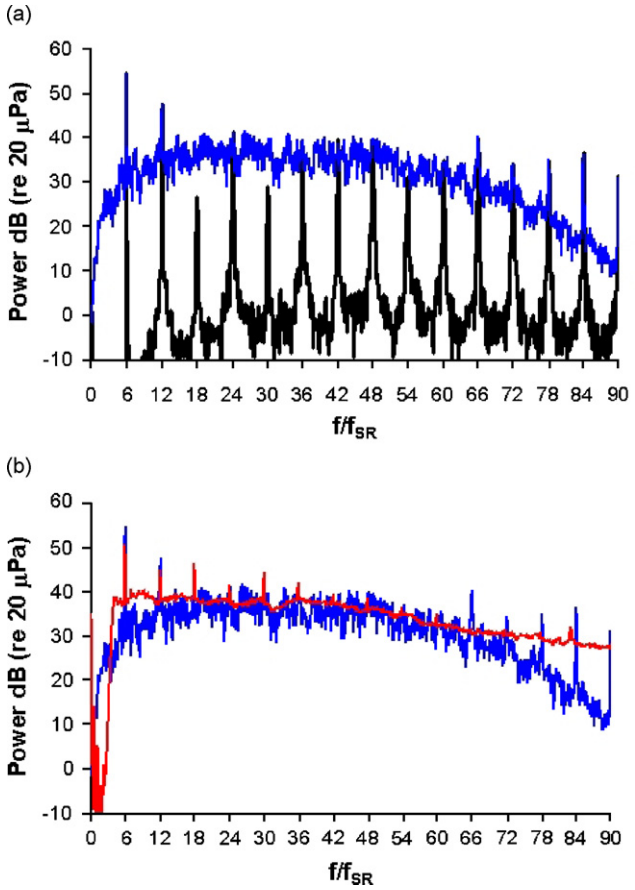

Fig. 13. Radiated noise estimates scaled to 1 meter. Experimental data are from Muench [9] compared with simulated radiated noise data using the current turbulent inflow model. turbulent inflow, baseline (no turbulence), experimental data.

vorticity dominated stator wakes result in more energy at the higher blade rates. Since the current model only simulates the turbulent velocity and is not physics based, it is not possible to accurately model these higher blade rates using this model.

3.1. Simulated turbulence correlation

The effect of simulated turbulence correlation was examined in the hope of better achieving agreement with the higher blade rate tonals. Physically, turbulence may be characterized as an ensemble of several vortex structures, each with its own length scale and circulation. For this reason, the velocity fluctuations the blade sees will not be completely random but will be correlated as a function of the vortex size and relative location. Vortices that are smaller than the blade spatial discretization will result in the higher frequency turbulence to be uncorrelated. Alternatively, vortices whose sizes are on the order of the blade (or larger) will be correlated over on the entire blade. Vortices whose sizes fall in between will be correlated on some parts of the blade, but not in others. Therefore, the phase angle (Ψ_n) should not be completely random but correlated as a function of frequency.

An algorithm was developed to effectively mimic this process. Phase angle was randomly set at an initial point along the blade. Phase angle for the other points on the blade was then a function of frequency and corresponding radial distance from the initial point. At a given frequency, all points lying within the corresponding radius were assumed to be correlated (e.g. phase varies linearly as a function of radius). For very low frequencies, the phase over the entire blade row would be correlated. As frequency increases, only the velocities on given sections of the blade would be correlated.

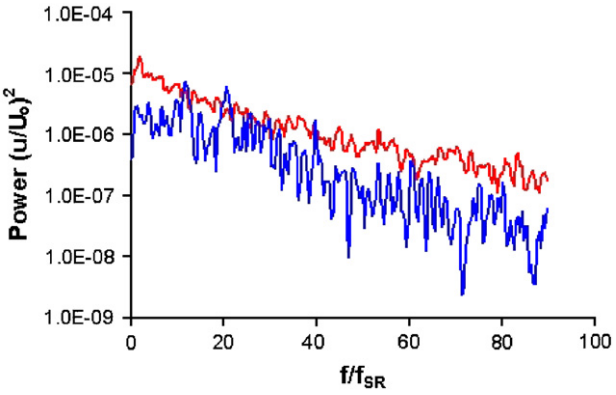

Fig. 14. Velocity power spectra based on simulated turbulent velocities taken in the hull boundary layer midway between two stators for the axial velocity component at $r/R_{prop} = 0.65$. ——— phase angle correlated based on model, ——— uncorrelated (random phase angle).

Fig. 14 shows a power spectra plot of the velocity field at $r/R_{prop} = 0.65$ between two stators comparing the correlated and uncorrelated axial velocities. As can be seen, the uncorrelated simulation shows a linear decrease that compares well with the experimental data presented in Fig. 9. The correlated data show a flat frequency response out to $f/f_{SR} = 20$. In addition, the spectra show a noisier response with multiple excursions in the spectra. While this plot does not show the correlation, it does show the effect of the correlation algorithm on the velocity field. The resulting computed force and radiated noise demonstrated similarly noisy behavior and did not agree nearly as favorably with experimental data. It is clear that more research is needed to better investigate these phenomena and will be the subject of future work.

4. Conclusions

A turbulent propulsor inflow model based on modulating the velocity inflow has been presented. The axial, radial and tangential velocity components are perturbed based on a broadband spectral input. The unsteady velocities are based on a Fourier series with the amplitudes experiencing an exponential decay with frequency. Experimental velocity spectral data were used to calibrate the inflow model. Velocity spectra appeared to have two separate regimes—the hull boundary layer regime and the stator wake regime. While both experienced a linear exponential decay with frequency, the hull boundary layer decay was steeper compared with the stator wake demonstrating that the stator wake has higher energy at the higher frequencies. As the edge of the boundary layer was approached, the corresponding boundary layer energy experienced further decay that was also modeled.

A modified propulsor unsteady flow code was used to compute the unsteady blade forces and pressures for fully unsteady turbulent inflow. Local blade forces demonstrated both tonal and broadband behavior illustrating the effect of the stator wakes. Except for the base tonal, the turbulent inflow model obfuscated the higher harmonics. For the global forces, however, it appeared that all of the blade rate tonals were obfuscated. Unfortunately, there were no data available to validate these observations.

It was possible to compute the far-field radiated noise based on unsteady surface pressure computations via the method of Goldstein to provide comparisons with experiment. Simulated data showed that the turbulent inflow model obfuscated all harmonics at the third blade rate and higher. Radiated noise was accurately predicted for the first two blade rate harmonics, as was the overall broadband component. The fact that the experimental data were "smoother" could be attributed to the number of averages that could be used due to the large amounts of data acquired. The fact that the higher harmonics were seen in the experimental data, but not the simulated data may be due to the fact that a non-physics-based model was used. This effect will be examined in more detail in future investigations.

The turbulent inflow model based on inflow velocity modulation appears quite effective in simulating the effect of turbulence on the blade forces as well as the far-field radiated noise. The fact that it is not physics based may affect the under-prediction of the higher blade-rate tonals. However, for many applications where

simulated turbulence is desired, this is a simple to implement, straight-forward methodology that can be inserted in many basic codes for the realistic prediction of unsteady propeller forces and radiated noise.

Acknowledgments

This work was funded by the Office of Naval Research under Contract N0001403WX20060, Dr. Kam Ng, program manager.

References

[1] M.M. Sevik, The response of propulsors to turbulence, *Proceedings of the Seventh Symposium on Naval Hydrodynamics*, Rome, Italy, August 1968, pp. 291–313.
[2] J.P. Wojno, T.J. Mueller, W.K. Blake, Turbulence ingestion noise, part 2: rotor aeroacoustic response to grid-generated turbulence, *AIAA Journal* 40 (2002) 26–32.
[3] P.D. Lysak, T.A. Brungart, Velocity spectrum model for turbulence ingestion noise from computational-fluid-dynamics calculations, *AIAA Journal* 41 (2003) 827–1829.
[4] J.E. Kerwin, Marine propellers, *Annual Review of Fluid Mechanics* 18 (1986) 367–403.
[5] S.A. Huyer, S.R. Snarski, Unsteady propulsor force prediction for spatially and temporally varying inflow, *ASME Paper No. FEDSM2002-31346, ASME Fluids Engineering Division Summer Meeting*, Montreal, Quebec, Canada, July 2002.
[6] S.A. Huyer, R. Kuklinski, Altering propulsor blade force response via inflow modulation, *Proceedings from the 2003 Undersea Defence Technology Europe*, Malmo, Sweden, June 2003.
[7] J.E. Kerwin, C.S. Lee, Prediction of steady and unsteady marine propeller performance by numerical lifting surface theory, *Transactions of the Society of Naval Architects and Marine Engineers* 86 (1978) 218–253.
[8] D.P. Keenan, Marine Propellers in Unsteady Flow, PhD Thesis, Massachusetts Institute of Technology, May 1989.
[9] J.D. Muench, Periodic Acoustic Radiation from a Low Aspect Ratio Propeller, PhD Thesis, University of Rhode Island, 2001.
[10] S.A. Huyer, S.R. Snarski, Analysis of turbulent propeller inflow, *ASME Journal of Fluids Engineering* 125 (2003) 533–542.
[11] T.S. Mautner, D.M. Nelson, M.C. Gillcrist, Investigation of the SISUP (swirl inducing stator upstream of propeller) concept for marine propulsion, Society of Naval Architects and Marine Engineers, *Proceedings: Propellers '88*, September 1988, pp. 2-1–2-12.
[12] C.J. Gedney, P.A. Abbot, P.J. Corriveau, Inferring blade rate forces from wind tunnel sound power measurements, *ASME Winter Annual Meeting, Symposium on Flow Noise Modeling, Measurement and Control*, November 1998, pp. 129–135.
[13] M.E. Goldstein, *Aeroacoustics*, McGraw-Hill, New York, 1976.